https://doi.org/10.5194/egusphere-2023-2694
Preprint. Discussion started: 10 April 2024

Post-fire Variability in Sediment Transport by Ravel in the Diablo Range

Hayden Jacobson[1], Danica L Roth[1], Gabriel Walton[1], Margaret Zimmer[2,3], Kerri Johnson,[4,5]

[1]Colorado School of Mines, Department of Geology and Geological Engineering, Golden, CO, 80401, United States
[2]University of California Santa Cruz, Department of Earth and Planetary Sciences, Santa Cruz, CA, 95064, United States
[3]U.S. Geological Survey, Upper Midwest Water Science Center, Madison, WI, 53726, United States
[4]University of California Berkeley, Department of Integrative Biology, Berkeley, CA, 94720 United States
[5]University of California Santa Barbara, UC Natural Reserve System, Santa Barbara, CA, 93106, United States

Correspondence to: Hayden L. Jacobson (jacobson@mines.edu)

Abstract. Post-fire changes to the transport regime of dry ravel, which describes the transport of individual particles downslope, are poorly constrained on a regional level but critical to understand as ravel may contribute to elevated sediment fluxes and associated debris-flow activity observed post-fire in the western United States. In this study, we evaluated post-fire variability in dry ravel travel distance exceedance probabilities and disentrainment rates through a series of field experiments simulating ravel with particles collected in situ. We conducted experiments between March 2021 and March 2022 on soil-mantled hillslopes in the Diablo Range of central coastal California following the Santa Clara Unit Lightning Complex fire of August 2020 with the goal of identifying a regime of "bounded" (light-tailed) or "runaway" (heavy-tailed or nonlocal) motion for different particle sizes between 3 and 35 mm. We conducted this study on both grassy south-facing slopes and oak woodland north-facing slopes. We tracked the post-fire evolution of particle transport regimes by fitting a probabilistic Lomax distribution model to the empirical travel distance exceedance probabilities of different particle sizes on a range of experimental slopes. Our experimental results indicated that a general transition from more runaway to more bounded transport occurred for our largest experimental particles (median intermediate axis of 28 mm) on south-facing slopes as vegetation recovered within the first year post-fire, while small and medium particles (median intermediate axes of 6 and 13 mm respectively) on south- or north-facing slopes and large particles on north-facing slopes did not experience notable changes in transport behavior. After the first year, seasonal variation in vegetation characteristics, such as grass density, appeared to control particle motion.

1 Introduction

The average yearly areal extent of burned land in the Western United States is increasing (e.g., Parks & Abatzoglou, 2020). Fire is an effective agent of weathering and results in the mobilization of sediment, with a temporary increase in sediment transport rates frequently observed post-wildfire (e.g., Roering & Gerber, 2005; Shakesby & Doerr, 2006; Swanson, 1981; Wondzell & King, 2003). It is critical to characterize the post-fire evolution of transport mechanisms that contribute to

https://doi.org/10.5194/egusphere-2023-2694
Preprint. Discussion started: 10 April 2024

changes in sediment transport rates, as it can inform our understanding of post-fire variability in catchment scale sediment loading and associated hazards, such as debris flows (e.g., DiBiase & Lamb, 2019; Florsheim et al., 1991; Jackson & Roering, 2009). Additionally, the form of hillslopes in steeplands is governed by the length scale of sediment transport and understanding post-fire sediment transport regimes informs the appropriate construction of long-term landscape evolution models (Tucker & Bradley, 2010).

A contributor to the observed post-fire increase in sediment transport in the Western U.S. is ravel, the rarified, gravity-driven transport of individual gravels or soil aggregates, collectively referred to here as "particles." Ravel is entrained by surface disturbances such as bioturbation or wildfire (Gabet, 2003; Jackson & Roering, 2009; Roering & Gerber, 2005). The incineration of vegetation dams during wildfires releases retained sediment on slopes greater than the angle of repose of the stored sediment, which then travels downslope as ravel (Bennett, 1982; Dibiase & Lamb, 2013). The loss of vegetation and associated surface roughness also results in reduced frictional resistance to the gravity-driven transport of ravel entrained in the months following a fire. This change may drive a transition between a distance-bounded particle motion regime defined by net kinetic energy loss via friction to a runaway motion regime defined by net kinetic energy gains through the conversion of gravitational energy (Furbish et al., 2021; Roth et al., 2020). On hillslopes, this transition has been observed to occur at slopes of 30-40 degrees and has often been described as a shift from local to nonlocal transport (DiBiase et al., 2017; Furbish et al., 2021a; Gabet, 2003; Gabet & Mendoza, 2012; Roering & Gerber, 2005). Nonlocal transport describes a condition in which the upslope topography influences the flux at a downslope position, as this "nonlocal" topography controls the motions of particles that are transported long distances (Foufoula-Georgiou et al., 2010; Furbish & Haff, 2010; Furbish & Roering, 2013). A theoretical transition between local and nonlocal transport can be described in terms of the form of the particle travel distance exceedance probability distribution (i.e., the complementary cumulative distribution of travel distances). As particle motion transitions from bounded (local) to runaway (nonlocal), the form of the travel distance exceedance probability transitions from light-tailed to heavy-tailed (Tucker and Bradley, 2010; Foufoula-Georgiou et al., 2010; Gabet & Mendoza, 2012; Roth et al, 2020). Since the sediment flux depends on the rate of particle entrainment and the distance particles travel before disentraining, the longer particle travel distances associated with nonlocal transport are expected to result in higher sediment fluxes (e.g., Furbish and Roering, 2013; DiBiase et al., 2017).

Recent experimental work suggests that nonlocal transport may occur at a lower gradient on smoother hillslopes (such as burned slopes) due to the decreased probability of particle disentrainment (DiBiase et al., 2017; Furbish et al., 2021b; Roth et al., 2020). Major increases in catchment-scale sediment yield due to ravel fluxes in the first year after fire have been well-documented in the Pacific Northwest (e.g., Swanson, 1981; Roering & Gerber, 2005; Jackson and Roering, 2009) and Southern California (e.g., DiBiase and Lamb, 2013; Florsheim et al., 1991; Lavé and Burbank, 2004; Lamb et al., 2011, 2013), where they have also been linked to post-fire hazards (e.g., DiBiase and Lamb, 2019; Guilinger et al., 2020; Kean et al., 2011; Wells, 1987). Very few studies have explicitly measured ravel fluxes after fire in Central California, and the

https://doi.org/10.5194/egusphere-2023-2694
Preprint. Discussion started: 10 April 2024

limited observations to date (Colins and Ketcham, 2001; East et al., 2021; Perkins et al., 2022) report relatively low fluxes compared to those in Southern California (Colins and Ketcham, 2001; East et al., 2021; Perkins et al., 2022). Even in the absence of fire, however, it has been shown that bioturbation-driven dry ravel has the potential to contribute significantly to long term hillslope evolution and hazards in Central California (e.g., Black and Montgomery, 1991; Reed and Amundson, 2007), highlighting the need for clarity on the mechanics and physical controls on ravel processes.

The recognition of nonlocal transport characteristics of ravel and the failure of traditional continuum-based diffusive transport models to describe the heavy-tailed distribution of travel distance exceedance associated with nonlocal transport has led to the development of alternative models to more effectively describe nonlocal transport (e.g., Furbish and Roering 2013). Recent field experiments demonstrate that ravel particle travel distances are consistent with the Lomax distribution model theorized by Furbish and Roering (2013) and refined by Furbish et al. (2021a). Using experimental clasts dropped on a range of burned and unburned field sites, Roth et al. (2020) showed that the parameters of a Lomax distribution capture a continuum of particle motion from local to nonlocal (i.e., light- to heavy-tailed distributions) as particle size increases or slopes get steeper or smoother. Furbish et al. (2021b) found that this model accurately described particle travel distances published in previous field experiments as well as new laboratory experiments. However, no study to date has conducted field experiments representative of natural particle motion in a manner allowing model validation against observed post-fire deposits or tracked the evolution of particle travel distances throughout post-fire recovery to explore the conditions under which dry ravel experiences nonlocal transport.

Here, we conduct a series of repeat particle drop experiments 7, 11, and 22 months post-fire at a total of seven positions on north- and south-facing hillslopes burned by the 2020 Santa Clara Unit (SCU) lightning complex fire in the Bay Area, CA. We fit experimental particle travel distances to a Lomax distribution model to assess spatial and temporal variation in particle motion as vegetation recovers over the year and a half following the fire. Our experiments are differentiated from prior studies by the use of experimental particles collected in situ at the field site and corroboration of results with particle size distributions measured along the study hillslope. We use our experimental results along with field measurement-based evidence of downslope coarsening of surface deposits to constrain the influence of particle size, surface gradient, and aspect-dependent vegetation loss and recovery on post-fire ravel fluxes.

1.1 Study Site

Our field experiments were conducted in Santa Clara County, California, USA at the Arbor Creek Catchment in the Blue Oak Ranch Reserve (BORR), an experimental ecological reserve managed by the University of California Natural Reserve System since 1990 (Fig. 1a). The experimental catchment is located in the Diablo Range of the California Coast Ranges and is underlain by the Yolla Bolly Terrain of the Franciscan Assemblage (Wentworth et al., 1999; Dibblee & Minch, 2006). Sandstone, meta-graywacke, and shale outcrops were observed at the field area (Donaldson et al., 2023). The Arbor Creek

https://doi.org/10.5194/egusphere-2023-2694
Preprint. Discussion started: 10 April 2024

Catchment has a drainage area of ~0.04 km^2 and elevation range of ~715-805 m a.s.l. The climate is Mediterranean, with warm, dry summers (August average 25°C) and cool, dry winters (January average 8°C). The majority of precipitation falls from October to May as rain (mean annual precipitation 600 mm), and streams are non-perennial (Donaldson et al., 2023).

The Arbor Creek Catchment consists of a generally south-facing slope (SFS) and a north-facing slope (NFS) draining to the west. The SFSis convex to planar with an average slope of 27 degrees and slopes up to 43 degrees adjacent to the channel. The NFS is planar to concave with an average slope of 31 degrees and slopes up to 35 degrees. Mobile material on the SFS generally consists of coarse, subangular to subrounded soil aggregates that move as coherent particles (Fig. 1b). On the NFS, the dominant species of mobile material is angular rocky colluvium, and a more limited fraction of soil aggregates is present relative to the SFS (Fig. 1b). The mineral surface of the NFS is more poorly consolidated and softer than at the SFS.

https://doi.org/10.5194/egusphere-2023-2694
Preprint. Discussion started: 10 April 2024

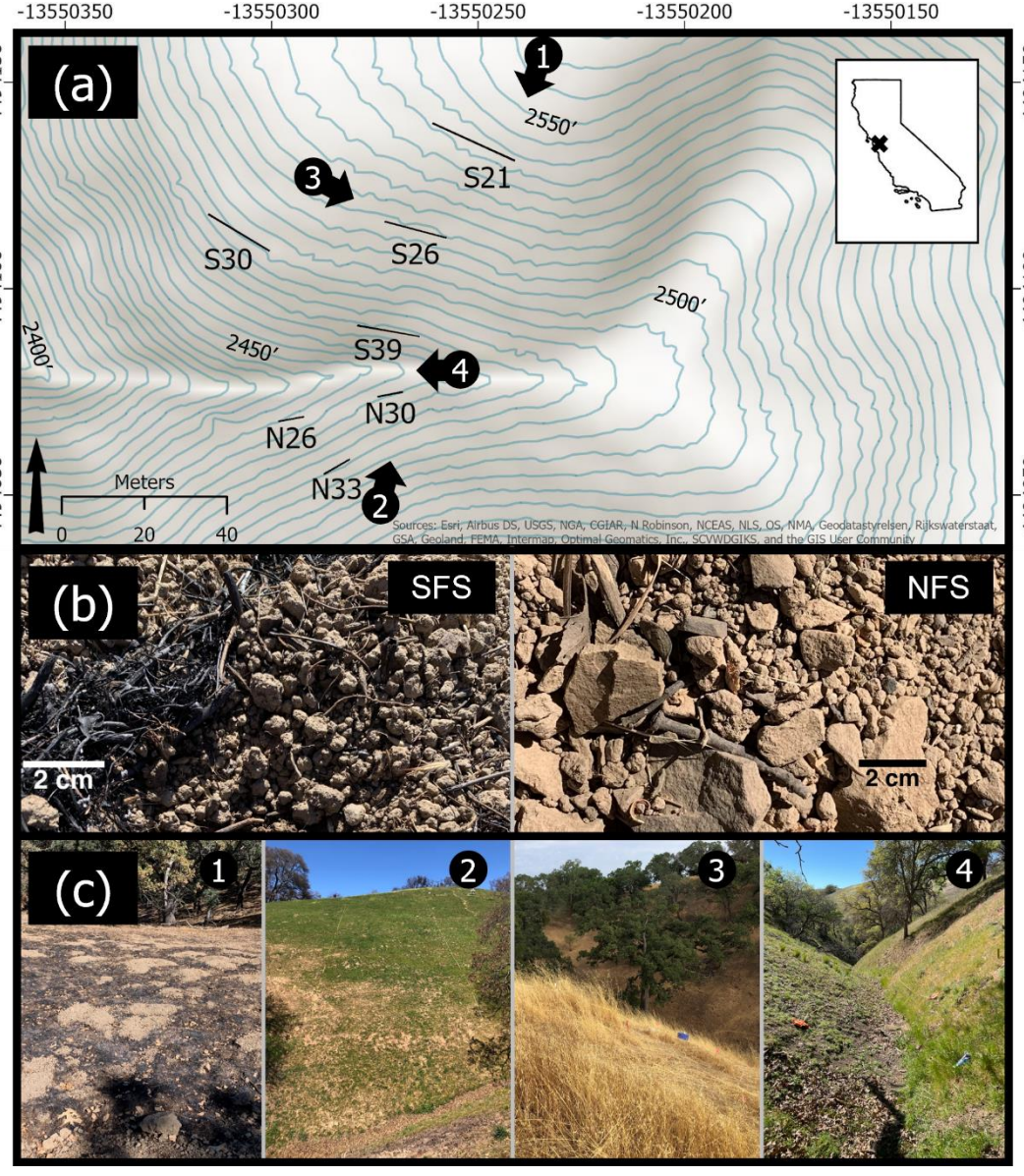

Figure 1: Row A: The inset map indicates the location of BORR within California. The primary map presents the layout of the particle drop lines for the 7 experimental sites in the Arbor Creek Catchment at BORR with elevation contours representing ~1.5 m (5 ft) intervals. Coordinates are displayed as UTM Northing and Easting, NAD 1983. Site labels reference aspect and average site slope angle (e.g., S21 corresponds to a south-facing site with slope of 21 degrees). The numbers 1-4 on the primary map indicate the location at which site photos (row C) were collected, with arrows representing photograph orientation. Row B: The images labeled SFS and NFS present the general post-fire condition of the surficial material at these slopes. Row C: Images (1-4) present various vantage points of the experimental catchment at different times including: one month post-fire (1), in Spring 2021 (2), in Summer 2021 (3), and in Spring 2022 (4). These photos exemplify the incineration (1) and initial recovery (2) of vegetation post-fire, followed by seasonal death (3) and regrowth (4).

https://doi.org/10.5194/egusphere-2023-2694
Preprint. Discussion started: 10 April 2024

Soils at this site extend to a depth of 30 to 80 cm, which is assumed to bound the activity of burrowing rodents on the slope (Donaldson et al., 2023). These include both California ground squirrels (Spermophilus beecheyi) and Botta's pocket gopher (Thomomys bottae). The SFS is dominated by annual grass species (e.g., Avena sp., Bromus diandrus). The NFS is dominated by blue (Quercus douglasii), black (Q. kelloggii), and valley (Q. lobata) oaks, with sparse annual grasses and prevalent lichens and moss. The grassy vegetation on these slopes undergoes seasonal cycles , with growth through the spring and senescence in late summer as rainfall ceases and temperatures increase. This is particularly noticeable at the SFS which receives more insolation and has a larger population of grasses relative to the NFS. We observed elevated antecedent soil moisture at the NFS relative to the SFS during all site visits (Donaldson et al., 2023).

During the August 2020 SCU Lightning Complex fire, grass was incinerated on the SFS. The depth of charred material was limited across the SFS, and grasses were singed down to a roughly uniform ~0-3 cm height, but generally still present at the soil surface. There was no alteration of granular aggregate structure or damage to fine root structure observed. Based on these characteristics and the observed recovery of vegetation within one year, the SFS was generally burned at low severity (Parsons et al., 2010).The NFS experienced a range of soil burn severities ranging from unburned to high, although the majority of the slope demonstrated low burn severity. Lichens and moss were observed to be unaltered in some areas post-fire. Limited patches of high burn severity were present where downed trees or branches were incinerated. Within these patches, the organic woody and soil components were completely consumed, several cm of white ash was present, and soils demonstrated disaggregation and oxidation typical of the extreme temperatures associated with burning of downed logs (e.g., Mataix-Solera, et al. 2011). On both NFS and SFS, the intensity of burrowing activity after the burn was clearly visible due to the difference in color of the charred surface and lighter excavated soil (Fig. 1c, Image 1).

Within 7 months of the fire, vegetation (grass) had begun to regrow on the SFS. During the March 2021 experimental period, the vegetation was several cm high and covered the majority of the SFS (Fig. 1c, Image 2). By July 2021 the SFS vegetation had experienced seasonal die-off, but residual dry matter ranged from roughly 30 cm to 1.3 m in height (Fig. 1c, Image 3). In March 2022, live vegetation had regrown to a height of several cm to 1 m and leaf litter and dead grasses were present on the mineral surface (Fig. 1c, Image 4). This material increased surface roughness relative to our first experimental period, as these materials had been recently incinerated in March 2021. The mineral and vegetative surface roughness in July 2021 and March 2022 qualitatively appeared very similar, though the height of the dead vegetation was greater in July 2021 and the the live vegetation was less brittle and more resistant to displacement when impacted by traveling particles in March 2022. The surface area of the vegetation acting as a barrier to the passage of particles was also greater in March 2022 due to the healthy, full stalks and leaves relative to the shriveled vegetation observed in July 2021.

https://doi.org/10.5194/egusphere-2023-2694
Preprint. Discussion started: 10 April 2024

The NFS experienced more limited post-fire evolution of vegetation compared to the SFS. During the experimental periods of July 2021 and March 2022 the surface characteristics of the NFS appeared similar based on vegetation density and moss cover, though more dead vegetation was present in March 2022 from the previous growing season.

2 Methods

2.1 Field Methods

Field visits occurred from September 2020 to March 2022, and experiments were conducted in March 2021, July 2021, and March 2022 (Fig. 1c, Images 2-4). In the following sections these three experimental epochs are described as Spring 2021, Summer 2021, and Spring 2022.

2.1.1 Wolman Counts and Particle Collection

Wolman counts (Wolman, 1954) consist of the random selection of loose particles at a given interval to obtain a distribution of in situ particle sizes. We performed Wolman counts to measure the intermediate axis of rocks or soil granules selected at intervals of 10 cm over 10 m contour-parallel transects on the south-facing slope. The Spring 2021 Wolman counts were conducted at three transects initially identified as capturing the variable slope of the SFS (S21, S26, S39) that were also used for rock drop experiments, described below. Particle measurements in Spring 2021 were conducted with a ruler, with 1 mm precision at S21 and S26 and 5 mm precision at S39.

The extent of subsequent Wolman counts in Summer 2021 and Spring 2022 was expanded to include 4 additional cross-slope transects, for a total of 7 transects spaced every 10 m downslope between the upper portion of the slope and the channel on the SFS. Particle measurements in Summer 2021 and Spring 2022 were conducted with a digital caliper, increasing measurement precision to 0.01 mm.

All in-channel particle measurements from Summer 2021 were collected above a leaf layer that accumulated in the months after fire, providing a lower bound to the timing of ravel deposition. The channel was then excavated down to the ash layer, such that all particle measurements from Spring 2022 represent material deposited between Summer 2021 and Spring 2022.

2.1.2 Particle Drops

Particle drop experiments were conducted at a total of 7 sites (Fig. 1a) to simulate ravel movement initiated by squirrel burrowing. The experiments in Spring 2021 were conducted in conjunction with the Wolman counts along only the three original SFS transects (S21, S26, S39). Initial experiments at these sites used only the randomly selected particles from the Wolman count, which were dropped immediately after measurement. To ensure adequate characterization of particle travel statistics across the full grain size distribution, additional ad hoc experiments were conducted at sites S26 and S39 with particles collected on-site and sorted into bins with 0.5-cm resolution.

https://doi.org/10.5194/egusphere-2023-2694
Preprint. Discussion started: 10 April 2024

The preliminary results of the Spring 2021 Wolman count were used to identify three particle size classes for future experiments to span the measured range of particle sizes. In Summer 2021 we collected and spray painted several hundred particles from the experimental hillslope (rocks or soil aggregates, i.e., granules) falling within three intermediate diameter ranges of 0.25-1 cm (small), 1-2 cm (medium), and 2-3.5 cm (large) for use in particle drop experiments (Fig. 2). These particles were used in all experiments conducted in Summer 2021 and Spring 2022. The grain size distribution of each particle group was later characterized by hand measurement in the lab with a digital caliper. Measured intermediate diameters for each size class fell within the ranges of 0.33-0.95 cm (small), 0.97-1.72 cm (medium), and 2.27-3.25 cm (large), with median (D50) values of 0.6, 1.3, and 2.8 cm, respectively for small, medium, and large particles (Appendix A, Table A2). We note that these values represent lower limits due to the possibility that some particles may have degraded in size without exceeding the particle size class limits. Based on the measured statistics of the particles used in Summer 2021-Spring 2022, we retroactively binned our data from Spring 2021 into small (0.25-0.75 cm), medium (0.75-2.25 cm), and large (2.25-3.25 cm) groups as comparable as possible to later epochs given the 0.5-cm precision of Spring 2021 measurements.

Under this binning criteria, a range of 41 to 230 particle travel distances were included for each experimental particle size class at S21, S26, and S39 in Spring 2021. At site S21, randomly selected particles of intermediate diameter larger than ~2.25 cm were not present in sufficient quantities to include a large particle class in our analysis. Table A2 in Appendix A contains additional information on experimental particles for all epochs.

https://doi.org/10.5194/egusphere-2023-2694
Preprint. Discussion started: 10 April 2024

Figure 2: Examples of small (left, blue), medium (middle, red), and large (right, pink) experimental particles used in particle drop experiments in Summer 2021 and Spring 2022. Ruler units are in cm.

In addition to the three sites selected in Spring 2021, four additional drop locations were selected in Summer of 2021 to capture a broader range of surface conditions. This includes a site at the western nose of the SFS (S30) and three sites on the NFS (N26, N30, and N33) as shown in Fig. 1a. The seven selected sites captured variation in aspect and slope over the study area. Particle drop experiments were conducted at all seven sites using the painted particles in Summer of 2021 and Spring of 2022 with a range of 100 to 200 particles dropped for each particle size class per site.

During the Summer 2021 experiments, grasses at the SFS experimental transects were observed to have heights of up to 1.3 m. At our experimental sites S21 and S26 these grasses were trimmed to ensure that particle distances could be feasibly measured and particles recovered after each experiment. Grasses were trimmed to ~15 cm, well above the estimated maximum particle bounce height at these sites, to avoid modifying the vegetative roughness encountered by the particles during transport.

During particle drop experiments, a tape measure placed contour-parallel using a clinometer defined a starting line along which particles were dropped at regular 10-cm intervals. Particles were dropped manually by releasing them from the middle of the palm with fingertips placed along the downhill edge of the starting line, resulting in randomized initiation of rotational particle motion following particle contact with the mineral surface (as recommended by Furbish et al., 2021b). Particle travel distances were measured in the slope-parallel direction using meter sticks or tape measures. Less than 5% of soil aggregate

https://doi.org/10.5194/egusphere-2023-2694
Preprint. Discussion started: 10 April 2024

particles degraded during transport (as evidenced by loss of paint) such that they fell outside of the selected particle size ranges and were removed from the experiment.

2.1.3 Topographic Data

Topographic data was collected by UNAVCO with a Riegl VZ-2000 terrestrial laser scanner (TLS) between July 18 and July 20, 2021. Registration and georeferencing of point clouds was performed by UNAVCO. Point cloud resolution was generally between 0.1-2 cm.

We used these point cloud data to define the surface slope at each particle experiment site. The software CloudCompare was used to fit a plane to the unmodified point cloud of each particle drop experimental region with the built in "Fit Plane" tool. Due to the low density of points corresponding to vegetation relative to points collected at the mineral surface in the experimental regions, the vegetation did not qualitatively appear to impact our slope estimation approach. All slope measurements were also corroborated with field measurements collected with a clinometer. The experimental regions were visually identified with survey flags placed in the field prior to TLS collection. The size of these selected regions was dependent on the width of the experimental drop zone and the maximum particle travel distance observed during the particle drop experiments described above.

2.2 Model Description

We used a Lomax model to represent particle travel distance exceedance probability R(x), also known as the survival function of particle travel distances or a complementary cumulative distribution. The exceedance probability can be related to an associated spatial disentrainment rate P(x), or hazard function representing the conditional probability of a particle in motion being disentrained at a distance x downslope from its point of entrainment. A Lomax distribution is capable of capturing both local and nonlocal transport regimes (Roth et al., 2020; Furbish et al., 2021), and generally acts as a constant function at low values of the travel distance, with a transition to a power law at greater values. This transition generally occurs at a value of B/|A| (Fig. 3) (Milojević, 2010).

The modeled forms of R(x) and P(x) are defined in terms of the Lomax shape (A, dimensionless) and scale (B, dimensions of length) parameters (Roth et al., 2020):

$$R(x) = \begin{cases} \left(\frac{Ax}{B} + 1\right)^{-1/A} & \text{for } A \neq 0 \\ \exp\left(-\frac{x}{B}\right) & \text{for } A = 0 \end{cases} \quad (1)$$

$$P(x) = \frac{1}{Ax+B} \quad (2)$$

The Lomax distribution can represent a range of forms of R(x) and P(x) as the transport regime transitions from local (A≤0) to nonlocal (A>0) (Fig. 3). The form of the R(x) and P(x) described by the shape parameter A informs our physical

https://doi.org/10.5194/egusphere-2023-2694
Preprint. Discussion started: 10 April 2024

understanding of the sediment transport regime. Although the Lomax distribution is fit to the survival function R(x) due to more limited potential for propagation of error from the cumulative probability distribution, the disentrainment function P(x) represents the physical process controlling travel distances and therefore informs our understanding of the mechanics of particle motion. Although our results are presented exclusively in terms of R(x) because these distributions were used to identify Lomax parameters A and B, we provide some background description of P(x) because of the physical relevance of the form of the distribution. R(x) explicitly results from P(x) and can be represented as such (Furbish and Roering, 2013).

$$R(x) = e^{-\int_0^x P(x')dx'} \quad (3)$$

The condition A<0 describing a light-tailed R(x) indicates that the likelihood of disentrainment P(x) will increase with distance asymptotically as particles approach position x=B/|A|. Particles are probabilistically unlikely to travel beyond this theoretical bounding distance, which we expect to increase with greater gravitational energy (for example, as grain size increases), an increased rate of conversion of gravitational energy to kinetic energy controlled by the surface gradient, and/or lower frictional losses from surface roughness. In this condition, B/(1-A) represents the mean travel distance (Furbish et al., 2021b). In this case, the model describes a transport regime of bounded motion, which is associated with "local" transport (Furbish et al., 2021b).

For A=0, R(x) is an exponential distribution and P(x) is equal to the constant 1/B, indicating the probability of disentrainment is equal at all travel distances and the transport regime can be described as uniform disentrainment. Regardless of the value of A, at short travel distances as $x \rightarrow 0$, $P \rightarrow 1/B$.

For A>0, the exceedance probability R(x) is heavy-tailed and the disentrainment rate P(x) decreases with distance along a slant asymptote P(x)=1/Ax after x=B/|A|. In this case, the spatially decreasing disentrainment probability represents the onset of runaway motion. The distance to this onset x=B/|A| is expected to decrease with greater gravitational energy (larger grain sizes) or conversion of gravitational to kinetic energy (steeper slopes) and lower frictional losses, each of which will lead particles to experience runaway motion at shorter distances. This condition represents the "nonlocal" transport regime (Furbish et al., 2021b).

https://doi.org/10.5194/egusphere-2023-2694
Preprint. Discussion started: 10 April 2024

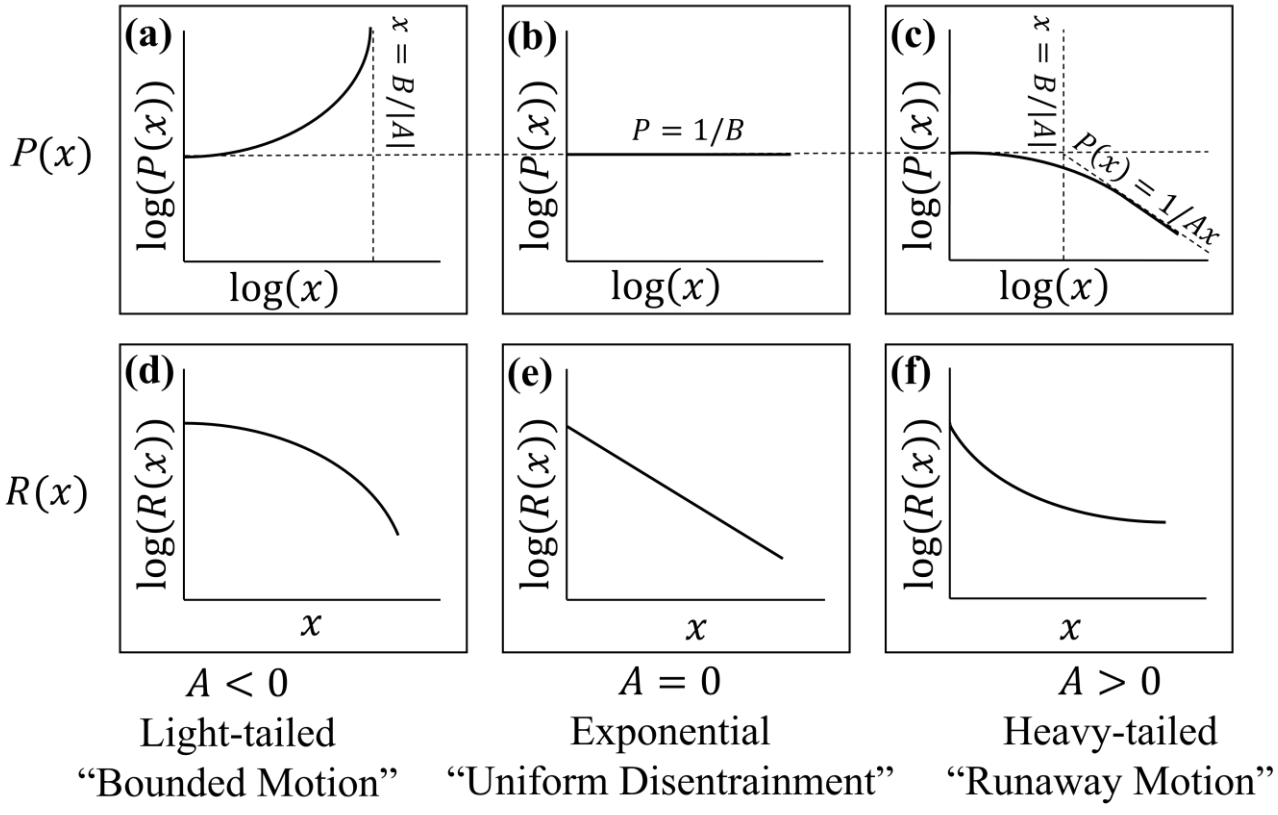

Figure 3: General form of the disentrainment rate P(x) (panels a, b ,c) and travel distance exceedance probability R(x) (panels d, e, f) corresponding to different values of the Lomax shape parameter (A) where x represents downslope travel distance, modified after Roth et al. (2020).

2.3 Initial Processing of Empirical Data

Preliminary processing of empirical travel distance data was conducted to prepare data for fitting the Lomax distributions. At very short distances prior to the onset of stochasticity, the disentrainment rate may be anomalously low relative to naturally occurring transport, especially for the smallest particles. To ensure that only the stochastic motion of each particle was captured and avoid the potential influence of unrealistically uniform initial particle velocities, we left-truncated all empirical travel distance exceedance distributions at a distance of 1 cm (i.e. removing travel distances ≤ 1cm). We note that the onset of stochastic motion may vary for particles of different geometry, as more rounded or angular particles may initially experience tumbling or a random oblique motion, respectively. We selected a single left truncation distance for combined distributions of different particle geometries rather than separating particles by geometry or composition (soil or rock) in order to achieve our goal of identifying a general trend for a given range of particle sizes. We selected the truncation value of

https://doi.org/10.5194/egusphere-2023-2694
Preprint. Discussion started: 10 April 2024

1 cm through a combination of visual analysis of the raw empirical R(x) data and consideration of the median intermediate diameter of the smallest particles involved in our study (~0.64 cm), which is approximately half the truncation distance (e.g., Furbish et al., 2020b).

After truncating travel distance measurements ≤ 1 cm, we calculated an empirical cumulative distribution, F(x) for each experimental travel distance dataset. We normalized F(x) by a factor of N+1 (where N is the number of samples) under the assumption that the cumulative probability of empirical data remains below 1 due to the finite number of samples (e.g., Furbish 2021b). Three of the seven sites were then assigned a Type-I (right) censor distance (Appendix A, Table A3) based on the distance to physical barriers that terminated particle travel such as the channel at the base of the slope (S39, all epochs), dense piles of vegetative debris (S30, Summer 2021), or trails caused by human activity on the slope (N33, Spring 2022). If a physical barrier was not present at the time of our experiments, then no Type-I censorship was applied. We then calculated the empirical exceedance distribution R(x) as the complementary cumulative distribution, or R(x) = 1-F(x).

2.4 Optimization of Lomax parameters

Lomax parameters describing the transport regime of our experimental ravel simulations were optimized by fitting a Pareto Type II (Lomax) distribution (Equation 1) to the empirical travel distance exceedance probability R(x). We optimized Lomax parameters A and B through an ordinary least-squares regression. Our approach is identical to that of Roth et al., (2020) with the Nelder-Mead Simplex selected for minimization, implemented as described in Lagarias et al. (1998). This algorithm is highly efficient, simple to implement, and capable of optimizing a wide range of objective functions. Because this method was not guaranteed to converge at a local minimum without an initial parameter estimation of reasonable quality, a trust region regression capable of handling poor initial guesses was first implemented to obtain initial estimates of A and B (Sorensen & Moré, 1983).

Error estimations presented in our results were calculated using a bootstrap procedure in which each R(x) was resampled with replacement 10000 times with one of the parameters A or B individually fixed while the other was calculated (per Roth et al., 2020). The standard deviations of the estimated parameters, σA and σB, respectively were used to denote their uncertainty, and the uncertainty in B/|A|, denoted σB/|A| was calculated through the method of moments using these standard deviations and the covariance of the bootstrapped parameters, σAB, as described in Equation 4.

$$\sigma_{\frac{B}{|A|}} = \sqrt{\left(\frac{B}{A^2}\sigma_{\mathrm{A}}\right)^2 + \left(\frac{1}{A}\sigma_{\mathrm{B}}\right)^2 - \frac{2B}{A^3}\sigma_{\mathrm{AB}}} \quad (4)$$

For cases in which nonlocal transport was identified with A>0, the tail is the sparsest region of the empirical data and may be underrepresented. This issue is exacerbated by a low sample number N. As noted by Furbish (2021b), parametric values estimated with N<1000 should be accepted with skepticism, especially for heavy-tailed distributions, for which variability in

https://doi.org/10.5194/egusphere-2023-2694
Preprint. Discussion started: 10 April 2024

R(x) increases. Any censored distributions may only have a small portion of the exceedance probability represented in the experimental data, exacerbating underrepresentation of the tail. Unfortunately, N>1000 was deemed to be impractical in our field experiments due to the extensive time required to drop, measure, and collect the in situ particles at a large number of sites as described in Sect. 2.1. This is a perspective shared by other similar field studies such as DiBiase et al. (2017), who dropped between 43 and 93 particles for their various size classes and Roth et al. (2020), who dropped ~100 particles of each size class per site. Given the logistical limitations of our experiments, we therefore acknowledge uncertainty in A, especially for low values of A~0. When assessing results in terms of a binary classification (i.e. A>0 versus A<0), to identify trends obscured by small values of A more likely to have an incorrect sign, we assessed the effects of filtering out values of $|A|<0.1$. This threshold was selected as representative of the calculated error for values of A~0 for which the median value was 0.087 over all sites, grain sizes, and experimental epochs.

3 Results

3.1 Wolman Counts

The particle size distributions measured by Wolman counts during each study epoch are presented in Fig. 4. The median diameter (D50) of our three selected particle size classes for Summer 2021 and Spring 2022 are indicated on all plots.

In Spring 2021, particle size distributions appear similar along all three transects at which measurements were collected (0 m, 20 m, and 50 m transects roughly corresponding to the positions of sites S21, S26, and S39). We note that because measurements taken along the 50 m transect near the hillslope toe were recorded at 0.5 cm precision, this distribution is only coarsely comparable with other distributions. In Summer 2021, we observe notable downslope coarsening in surface particles in the lower transects near the hillslope toe where slopes increase. The material collected at “channel S”, or the channel along the base of the SFS, was coarser than the material on the hillslope, with a median value over twice that of the lowest hillslope transect at 50 m (Appendix A, Table A1). By Spring 2022, downslope coarsening at the toe was still evident, but had declined substantially.

https://doi.org/10.5194/egusphere-2023-2694
Preprint. Discussion started: 10 April 2024

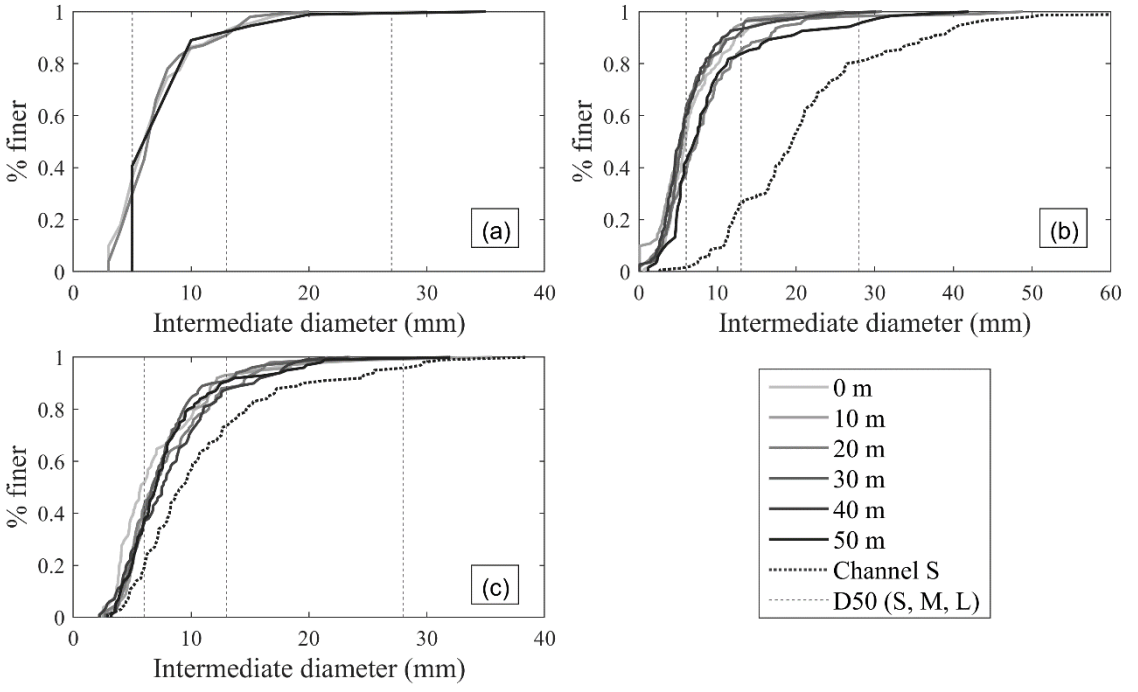

Figure 4: Particle size distributions from Wolman counts conducted on cross-slope transects along the study hillslope during each epoch. Distances 0 - 50 m represent each transect's downslope distance from experimental particle drop site S21. The extent of counts in Spring 2021 was limited to only 0, 20 and 50 m transects, and particle sizes at 50 m were collected at a reduced measurement precision (0.5 cm). Dashed lines represent the median diameters (D50) of the three particle size groups used in Summer 2021 and Spring 2022 experiments (S = 0.6 cm, M = 1.3 cm, and L = 2.8 cm).

3.2 Evolution of A with Site Recovery

Figures 5 and 6 show variation in model R(x) through time for each experimental site and grain size combination (see Appendix B, Fig. B1-B7 for individual empirical datasets, model fits and resulting Lomax parameter values). Figure 5 indicates the evolution of R(x) at all SFS sites while Fig. 6 shows the evolution of R(x) at all NFS sites. Note that experiments at sites on the NFS and the S30 site were only conducted in Summer 2021 and Spring 2022.

https://doi.org/10.5194/egusphere-2023-2694
Preprint. Discussion started: 10 April 2024

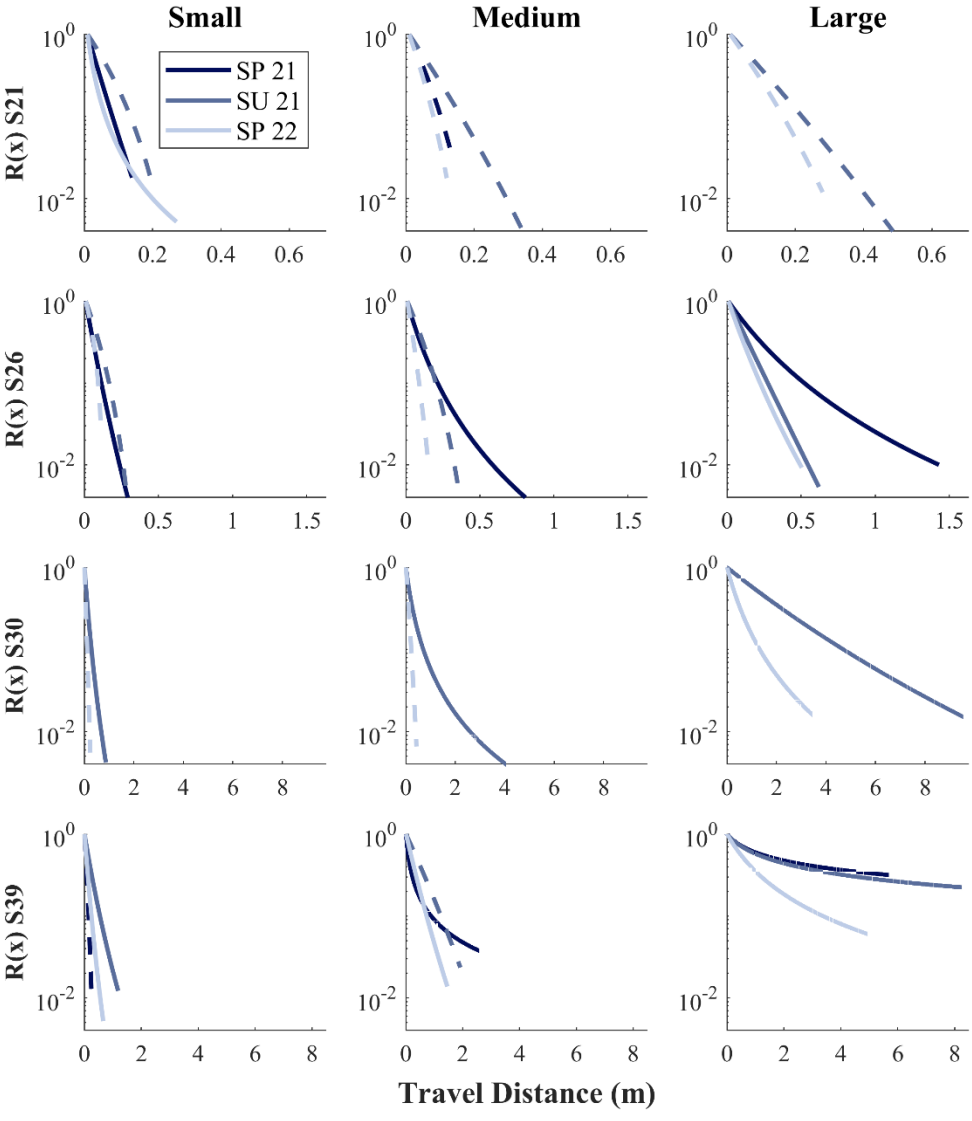

Figure 5: Modeled travel distance exceedance distributions R(x) for all SFS sites. Dashed lines indicate A<0 (bounded motion) and solid lines indicate A>0 (runaway motion). Columns correspond to particle sizes (small, medium, large) while rows indicate experimental site.

365

https://doi.org/10.5194/egusphere-2023-2694
Preprint. Discussion started: 10 April 2024

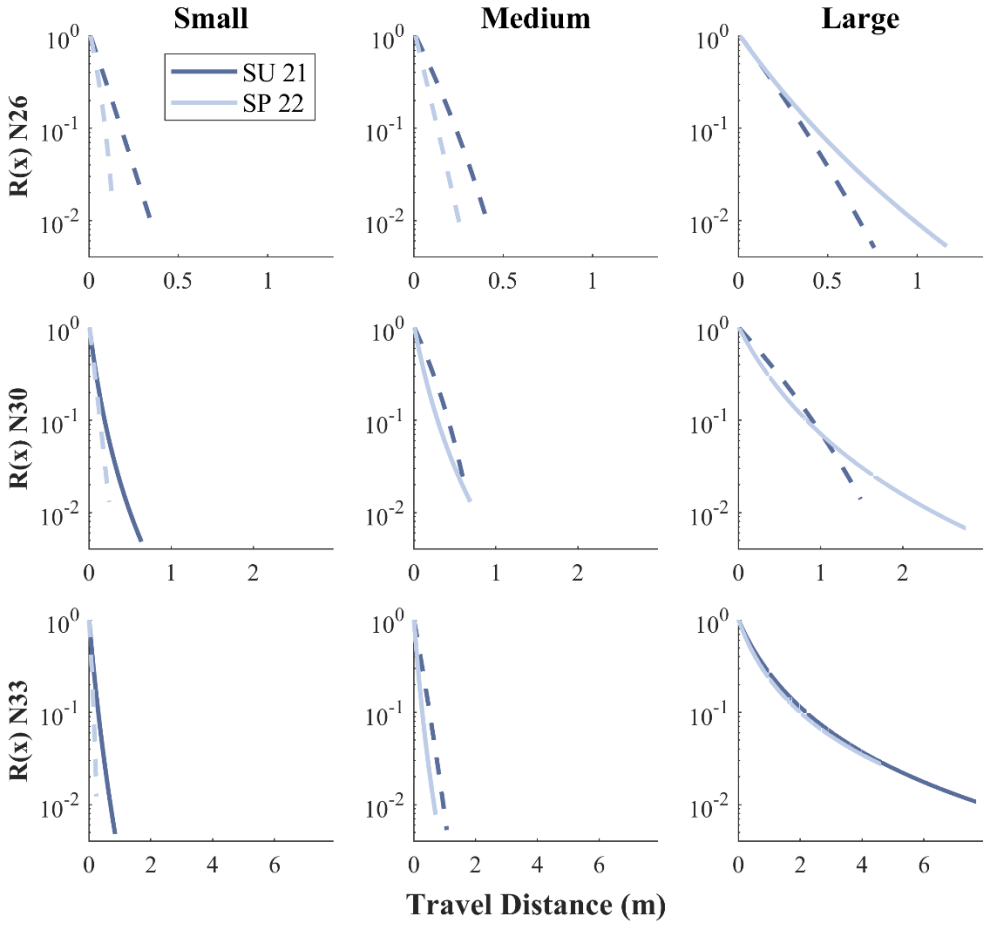

Figure 6: Modeled ravel distance exceedance distribution R(x) for all NFS sites. Dashed lines indicate A<0 (bounded motion) and solid lines indicate A>0 (runaway motion). Columns correspond to particle sizes (small, medium, large) while rows indicate experimental site.

Figures 5 and 6 indicate that nonlocal transport of the in situ grains in our experimental catchment occurs across a range of grain sizes, slopes, and aspects as evidenced by the presence of heavy-tailed travel distance exceedance distributions (solid lines). In Fig. 5, heavy-tailed distributions at the SFS are shown to be most prevalent for the largest particles, and their occurrence decreases for smaller grain sizes. More heavy-tailed distributions are also observed across the range of slopes and grain sizes in the first experimental periods during earlier stages of post-fire site recovery, with a general transition to light-tailed distributions as the site continued to recover. Results using a 1.75 cm M/L binning threshold rather than 2.25 cm for Spring 2021 are presented in Table A4.

https://doi.org/10.5194/egusphere-2023-2694
Preprint. Discussion started: 10 April 2024

Figure 6 does not display the general temporal trends that can be seen in Fig. 5, but similarly indicates that heavy-tailed distributions of travel distance exceedance at the NFS were more likely to occur for larger grains at steeper slopes. No single trend in A vs. time elapsed since the fire can be consistently identified across all sites and particle sizes. As noted in Sect. 2.4, the uncertainty inherent to A calculated at a relatively low sample sizes (especially with small values of A~0) means that caution should be exercised in drawing conclusions from a single site. We therefore consider the net evolution of A by comparing the mean A values for each size class and experimental epoch over all north- or south-facing sites. To better understand the observed changes in the distribution shape parameter A through our experimental epochs, the aggregate evolution of A for small, medium, and large particles was assessed with all values included and only values of |A|>0.1 (Fig. 7).

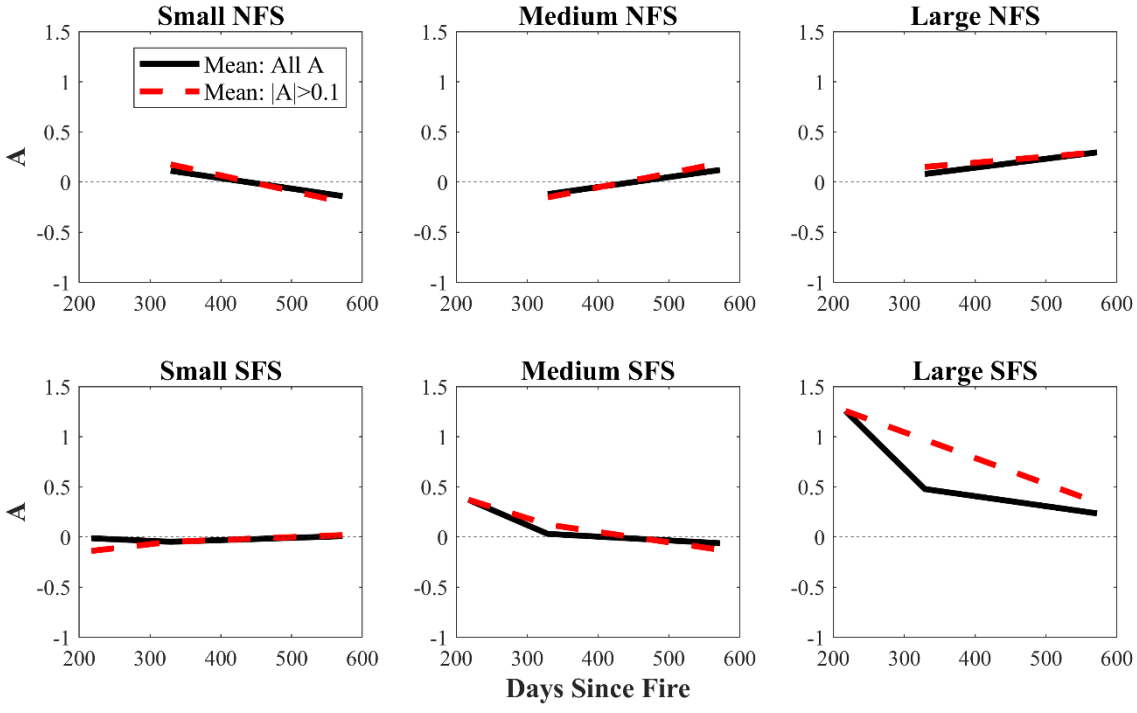

Figure 7 Trends in Lomax shape parameter A (mean value) with time for each size class over all experimental sites separated by aspect. The solid black lines represent trends with all A values, while the dashed red lines show trends for |A|>0.1 only. Field visits occurred 217, 329, and 572 days post-fire.

The most notable trend presented in Fig. 7 is the continuous decrease in A for the largest particles at the SFS. Fig. 7 shows opposite trends for medium and large particles between Spring 2021 and Summer 2022 at the NFS and SFS slope, with a transition to more light-tailed distributions at the SFS and a transition to more heavy-tailed distributions at the NFS. Very limited variation in the behavior of small particles at the SFS was observed through the three experimental periods, and small particles at the NFS transitioned to more bounded motion between Spring 2021 and Summer 2022.

https://doi.org/10.5194/egusphere-2023-2694
Preprint. Discussion started: 10 April 2024

We also note that, due to both the slight misalignment between the particle size bins used during Spring 2021 and later experimental epochs, as well as the possibility that some painted experimental particles experienced experimental wear before measurement, the A values presented for Spring 2021 may be skewed toward slightly smaller particles than later epochs for small and large particles, and include a slightly larger upper limit on medium particle sizes.

4 Discussion

Our experimental particle drop results provide clear evidence of nonlocal transport as indicated by heavy-tailed travel exceedance distributions recorded for a variety of grain size and slope combinations. Since these results represent the behavior of in situ particles under experimental conditions intended to simulate a primary particle entrainment process at this site (burrowing), these results suggest that nonlocal transport does occur within the natural range of grain sizes, slopes, and post-fire surface conditions at this site. Additionally, we observed a general transition from lighter tails to heavier tails as particle sizes increased, consistent with expected controls on particle disentrainment (e.g., Roth et al., 2020; Furbish et al., 2021a), as larger particles have a larger component of effective gravitational energy (larger D50). On the SFS, we observed nonlocal transport of medium and large particles at all sites with slopes of 26 degrees or greater in Spring 2021 (Fig. 5). At S26 and S39, a transition from nonlocal to local transport was observed between Spring 2021 and Summer 2021 for medium particles while large particles still experienced nonlocal transport. After Summer 2021, systematic changes in particle motion are not observable across all SFS experiments, but the maximum particle travel distance decreased for all SFS sites and all grain sizes. The post-fire observation of downslope coarsening along the SFS hillslope and the coarser particles found in the channel relative to the SFS hillslope (Fig. 4, Appendix A Table A) provide evidence of particle size-selective transport consistent with our experimental results. Previous field experiments and observations of post-fire dry ravel (Florsheim et al., 1991; Gabet, 2003; Roering and Gerber, 2005; Lamb et al., 2013; DiBiase et al., 2013, 2017; Roth et al., 2020) report the sequestration of fine sediments by mineral or vegetative roughness as large particles bypass hillslope storage zones and are delivered to the channel network. This mechanism produces the variation between hillslope and channel particle size distributions in Fig. 4. Combining our experimental results with the observed evolution in down-slope particle size distributions, we infer the following speculative interpretation of events on the south-facing slope following the fire. Although particle size distributions from the toe slope were measured at lower precision in Spring 2021, they showed no indication of the downslope coarsening observed at this site by Summer 2021. This early relative depletion of the coarsest fraction suggests that the largest particles were evacuated from the hillslope during or immediately after the fire. We observed intense burrowing activity on the slope approximately one month post-fire (Fig. 1c, Image 1) that resulted in freshly excavated material being supplied to the hillslope post-fire, including large particles that replenished the deposit size distributions over time. The decline in downslope surface coarsening between Summer 2021 and Spring 2022 along with the shift from heavier- to lighter-tailed experimental travel distances suggests that particle motion was recovering within the first

https://doi.org/10.5194/egusphere-2023-2694
Preprint. Discussion started: 10 April 2024

year and a half following the fire. Within that period, however, nonlocal transport continued to preferentially move larger particles farther downslope, first leading to relative over-enrichment of the coarser fraction at the toe and gradually replenishing coarse particles from the toe up as vegetation regrew and nonlocal transport progressively declined. Between Summer 2021 and Spring 2022, vegetation recovered enough for seasonal variation to obscure any remaining impact of recovery on experimental travel distances for all but the largest particles and steepest slope.

Between Summer 2021 and Spring 2022 at the NFS we observe a slight decrease in A for small particles, whereas medium and large particle drop experiments demonstrate a small increase in A (Fig. 6). No experiments were conducted at the NFS in Spring 2021, which limits our ability to understand how transport evolved on the slope as the catchment's vegetation recovered through the first year post-fire. While some component of post-fire recovery was likely occurring during our experimental periods in Summer 2021 and Spring 2022, it is possible that seasonal controls on vegetation were more influential in these NFS experiments. In Spring 2022 the vegetation was qualitatively observed to be shorter and sparser at the NFS than the SFS as the growing season had not ended and the NFS was more obscured by shadow due to aspect and tree cover. Medium and large particles were apparently more able to pass over the structure of this vegetation than small particles, inducing an overall increase in A for the larger particle classes. Motion of the small particles also appeared to be more hindered by dead vegetation from the prior year, causing the shift to more bounded transport in Spring 2022 at the NFS. The variable shifts in transport regime between the NFS and SFS between Summer 2021 and Spring 2022 suggests that aspect-dependent differences in vegetation types and seasonal changes in vegetation and had already differentiated the post-fire effects on ravel transport on the north- and south-facing slopes within 11 months of the fire. As shown in Fig. 7, experiments with small and medium particles exhibited no obvious trend in A as the site recovered even when displayed in aggregate. Variability in A during initial recovery is most apparent for large particles at the SFS between Spring 2021 and Summer 2021 during which they exhibited a transition from nonlocal transport to near uniform disentrainment (A=0). While only considering $|A|>0.1$, the mean value of A exhibited a more linear evolution through the three experimental periods for large particles at the SFS. This result is also visible in Fig. 5, and suggests that the largest particles present at our site experienced a more noticeable transition in transport regime than smaller particles post-fire. The regrowth of vegetation generally results in increased roughness and an accompanying increase in frictional losses, which we interpret as causing experimental travel distance distributions to shift toward lighter tails over time for the largest particles at the SFS. These findings are consistent with the observed reduction in downslope coarsening of hillslope and channel deposits over time (Fig. 4), indicating that preferential transport of larger particles generally decreased as vegetation recovered. Regardless of filtering of A values, Fig. 7 shows that experiments conducted over 1.5 years after the fire at the SFS indicate nonlocal transport of the largest grains was still occurring. We can infer from these results that nonlocal transport may be a longer-term process than the timescale of primary post-fire recovery.

https://doi.org/10.5194/egusphere-2023-2694
Preprint. Discussion started: 10 April 2024

While specific sites such as S26 exhibited a continuous transition from heavier- to lighter-tailed distributions between Spring 2021 and Summer 2021 for all particle sizes, no consistent transition from more runaway to more bounded motion could be identified across all sites. When considering these results it is important to be aware that regressed A values generally represent an upper bound estimate of A due to potential overfitting of tails, which are generally the sparsest region in our empirical data. This issue is exemplified by the potential removal of the farthest travel distance recorded at S21 in Spring 2022 for small grains (Appendix B, Fig. B1), which would modify the R(x) distribution from one describing runaway motion (unrealistic at this site for small grains given our other results) to near uniform disentrainment. At some sites for which error was large relative to the calculated A value, it was difficult to distinguish clear signals in the transport regime over noise, which we assume was dominated by seasonal vegetation or resulted from under-sampling issues. Further experiments would be required to constrain the background level of travel distances at an unburned site or over longer time periods to validate whether this catchment had fully recovered by Spring 2022, but the general decrease in net travel distances throughout our experimental epochs at the SFS indicates that post-fire recovery may have continued to occur nearly two years after the area was burned.

5 Conclusion

This study examines post-fire variability in rarified particle motion representative of dry ravel at Arbor Creek Catchment at Blue Oak Ranch Reserve in the Mt. Diablo Range of the California Bay Area. We conducted a series of particle drop experiments using in situ particles in size classes representative of the range of particle sizes present at our field site, as measured by Wolman pebble counts along cross-slope transects. We fit our experimental particle travel distances to a Lomax distribution model for the travel distance exceedance probability of simulated ravel, in order to track the post-fire evolution of the form of these distributions with time, particle size, and slope, and aspect. The results of our particle drop experiments indicate that nonlocal transport occurred for medium to large particles ($\gtrsim$1 cm) on slopes $\gtrsim$26° for at least 6 months to a year following the fire, consistent with downslope coarsening in grain size distributions measured along-slope and in the channel below the study hillslope.

To our knowledge, these findings constitute the first quantitative documentation of naturally occurring nonlocal transport occurring after wildfire. The evolution of the Lomax parameter A, which describes the form of the travel exceedance distribution as light-tailed (bounded motion, local transport) or heavy-tailed (runaway motion, nonlocal transport) generally reflected a transition from heavier- toward lighter-tailed travel distance distributions within 11 months of the fire on south-facing slope aspects, accompanied by a shift toward shorter experimental particle travel distances. Conversely, we observe no clear temporal trends on the mossy, oak-covered north-facing study slope. Our results suggest that vegetation and soil differences reflecting antecedent moisture and aspect-dependent insolation differences may drive distinct post-fire dry ravel fluxes on north- and south-facing hillslopes.

https://doi.org/10.5194/egusphere-2023-2694
Preprint. Discussion started: 10 April 2024

Appendix A: Experimental grain and site parameters

Table A1: Hillslope particle size statistics. Median, minimum, maximum, standard deviation and number of measurements collected by Wolman counting on cross-slope transects along the study hillslope during each epoch. Transect position describes the downslope distance from Site S21, or the channel at the base of the south-facing slope. In Spring 2021, measurements at 0 and 20 m were recorded with 1 mm precision, measurements at 50 m were recorded with 5 mm precision. In Summer 2021 and Spring 2022 measurements were recorded with 0.01 mm precision.

Transect position (m)	Epoch	Intermediate diameter (cm)				N particles
		Median	Min.	Max.	Std. dev.	
0	SP 21	0.6	0.3	3.0	0.4	111
	SU 21	0.593	0.066	2.371	0.411	111
	SP 22	0.575	0.236	2.312	0.418	102
10	SP 21	--				
	SU 21	0.55	0.01	2.611	0.428	111
	SP 22	0.678	0.255	3.550	0.470	100
20	SP 21	0.7	0.3	2.0	0.3	100
	SU 21	0.740	0.010	4.883	0.713	109
	SP 22	0.670	0.269	2.160	0.403	100
30	SP 21	--				
	SU 21	0.547	0.010	3.09	0.467	111
	SP 22	0.673	0.276	2.348	0.365	100
40	SP 21	--				
	SU 21	0.523	0.010	3.016	0.468	110
	SP 22	0.759	0.222	2.333	0.438	100
50	SP 21	--	0.5	3.5	--	91
	SU 21	0.717	0.118	4.194	0.767	121
	SP 22	0.703	0.323	3.198	0.460	100
Channel (S)	SP 21	--				
	SU 21	1.951	0.268	8.827	1.206	150
	SP 22	0.925	0.292	3.843	0.683	100

https://doi.org/10.5194/egusphere-2023-2694
Preprint. Discussion started: 10 April 2024

Table A2: Median, minimum, maximum, and standard deviation of grain sizes for all experimental particle classes. Particle minimum and maximum values are reported as bin edges for Spring 2021 due to measurement imprecision, and as measured sample minimum and maximum for summer 2021 and Spring 2022, during which pre-collected and painted particles were used.

Epoch	Site	Particle size class	Intermediate diameter (cm)				N
			Median	Min. (≥)	Max. (<)	Std. Dev.	
Spring 2021	S21*	Small	--	0.25	0.75	--	68-214
	S26	Medium	--	0.75	2.25	--	41-230
	S39	Large	--	2.25	3.25	--	42-58
Summer 2021 Spring 2022	all sites	Small	0.63	0.33	0.95	0.11	89-199
		Medium	1.31	0.97	1.72	0.16	93-200
		Large	2.80	2.27	3.14	0.18	97-204

*No particles in large size class dropped at site S21, Spring 2021

Table A3: Censor distances for all sites. Site S30 was censored in Summer 2021 only, Site N33 was censored in Spring 2022 only, and Site S39 was censored in all three epochs. The variable censor point at S39 caused by the variable distance to the sloping channel at the base of the site required manual censorship based on drop position.

Site	S21	S26	N26	S30	N30	N33	S39
Censor Distance (m)	None	None	None	10.5	None	7.5	6.2-8.6

Table A4: Comparison of Lomax parameter A resulting from alternative division of medium (M) and large (L) particle classes for relevant experiments conducted in Spring 2021. The classification of several particles recorded as 1.75 cm (i.e., falling between 1.5 and 2 cm) and 2 cm (1.75 - 2.25 cm) in diameter was particularly sensitive to our selection of the binning threshold between medium and large size classes. We tested thresholds of 1.75 and 2.25 cm for comparison, and found that a boundary of 2.25 cm resulted in less severe under sampling of the medium class at S39 without meaningfully altering results for the large particle class. We also note the that the lower edge of the Spring 2021 medium bin (0.75 cm) falls below the medium size range in the later epochs (0.97 cm). Given these considerations, we selected the 2.25 cm threshold for all analyses presented in the main text.

M/L Bound	S21 M	S26 M	S26 L	S39 M	S39 L
A value with L ≥ 1.75 cm	-0.19	0.20	0.21	0.07	1.98
A value with L ≥ 2.25 cm	-0.17	0.26	0.25	1.03	2.26

https://doi.org/10.5194/egusphere-2023-2694
Preprint. Discussion started: 10 April 2024

Appendix B: Detailed regression with empirical data and error for all sites

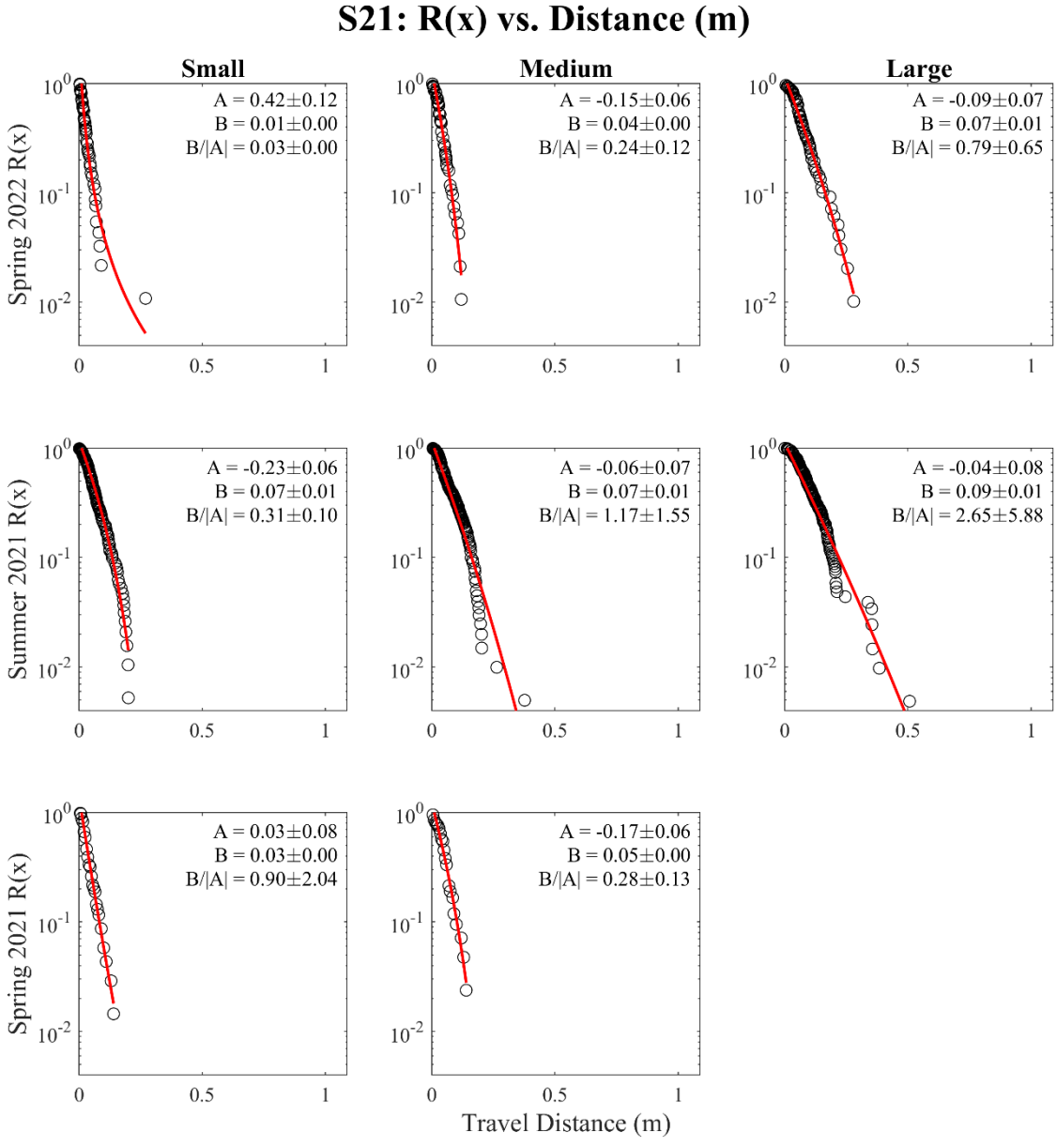

Figure B1: Empirical R(x) and modeled R(xi) for site S21 annotated with Lomax parameters A and B and characteristic distance B/|A|. Error estimations are denoted with parameter values. Black circles are empirical data.

https://doi.org/10.5194/egusphere-2023-2694
Preprint. Discussion started: 10 April 2024

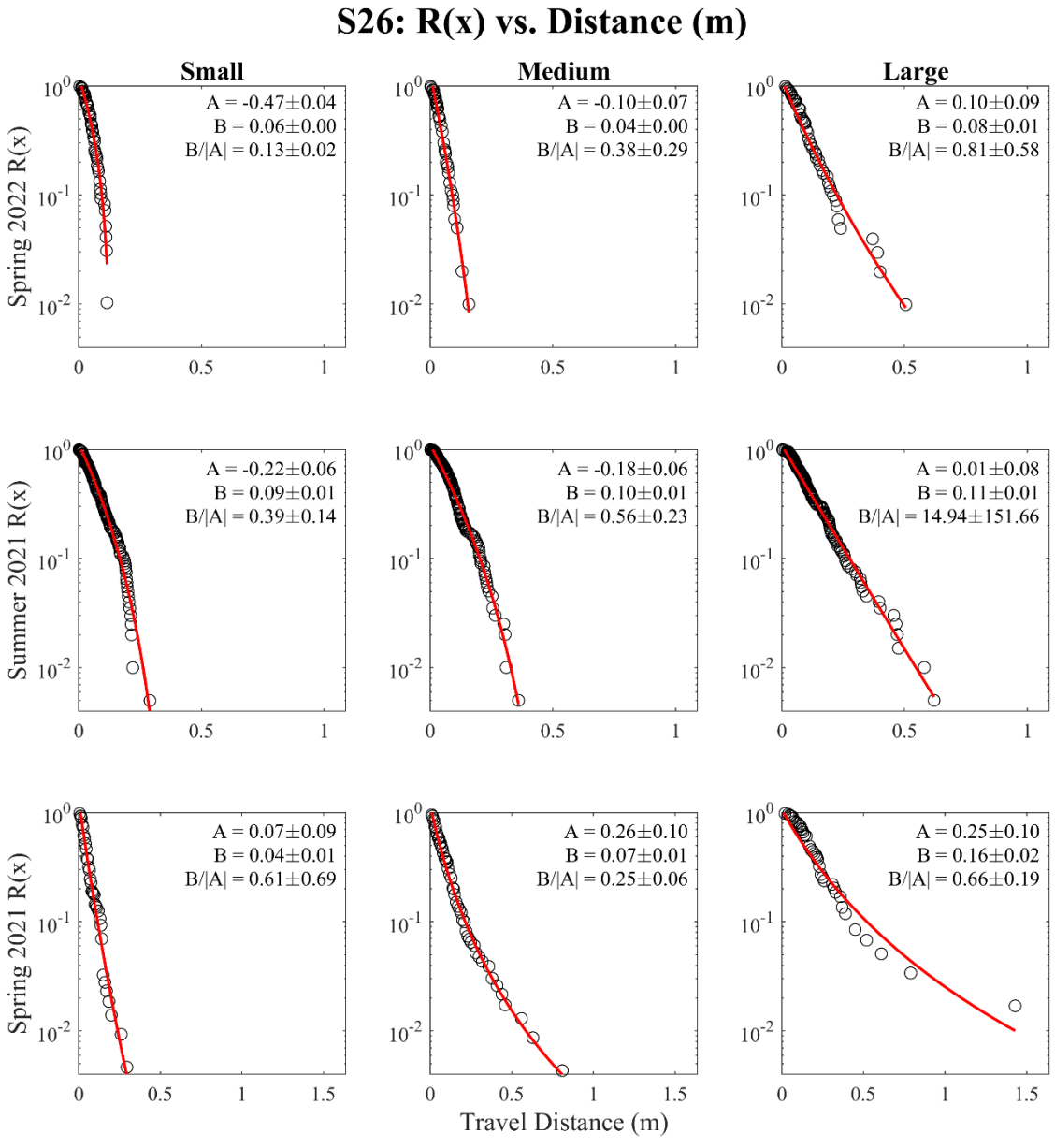

Figure B2: Empirical R(x) and modeled R(xi) for site S26 annotated with Lomax parameters A and B and characteristic distance B/|A|. Error estimations are denoted with parameter values. Black circles are empirical data.

https://doi.org/10.5194/egusphere-2023-2694
Preprint. Discussion started: 10 April 2024

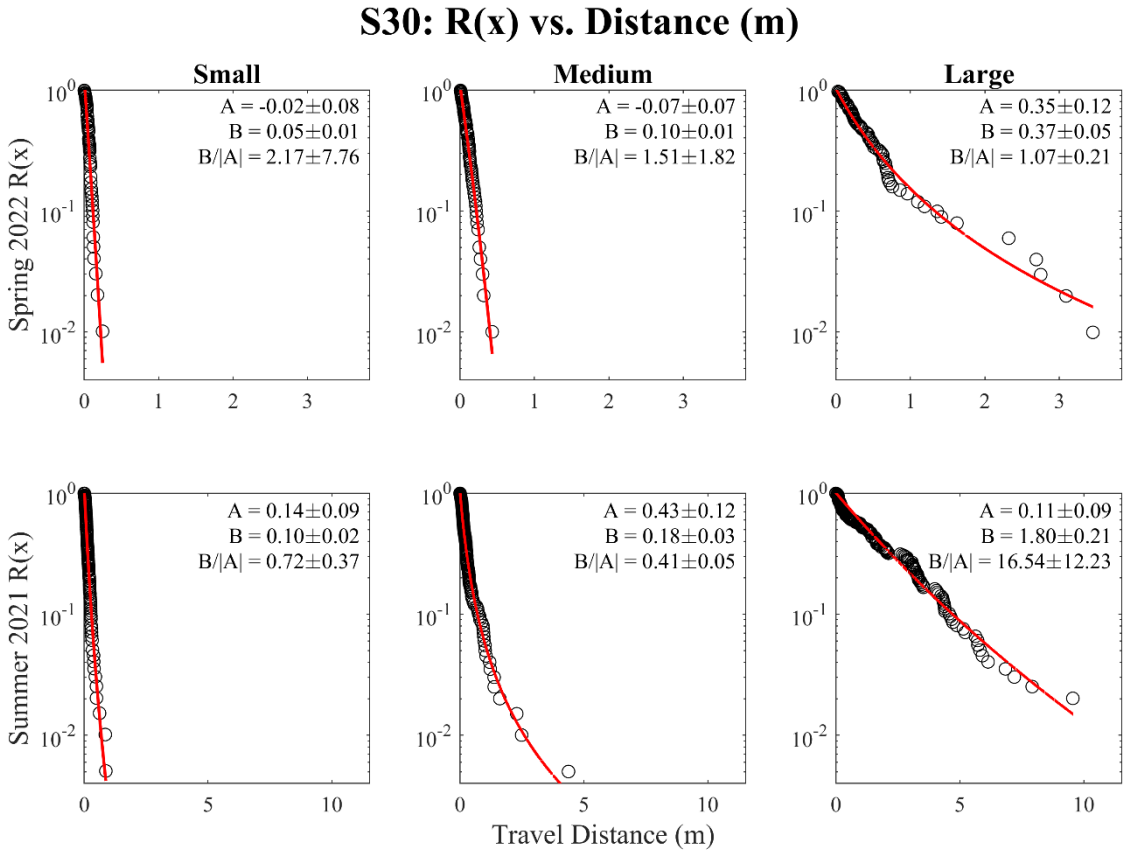

Figure B3: Empirical R(x) and modeled R(xi) for site S30 annotated with Lomax parameters A and B and characteristic distance B/|A|. Error estimations are denoted with parameter values. Black circles are empirical data.

https://doi.org/10.5194/egusphere-2023-2694
Preprint. Discussion started: 10 April 2024

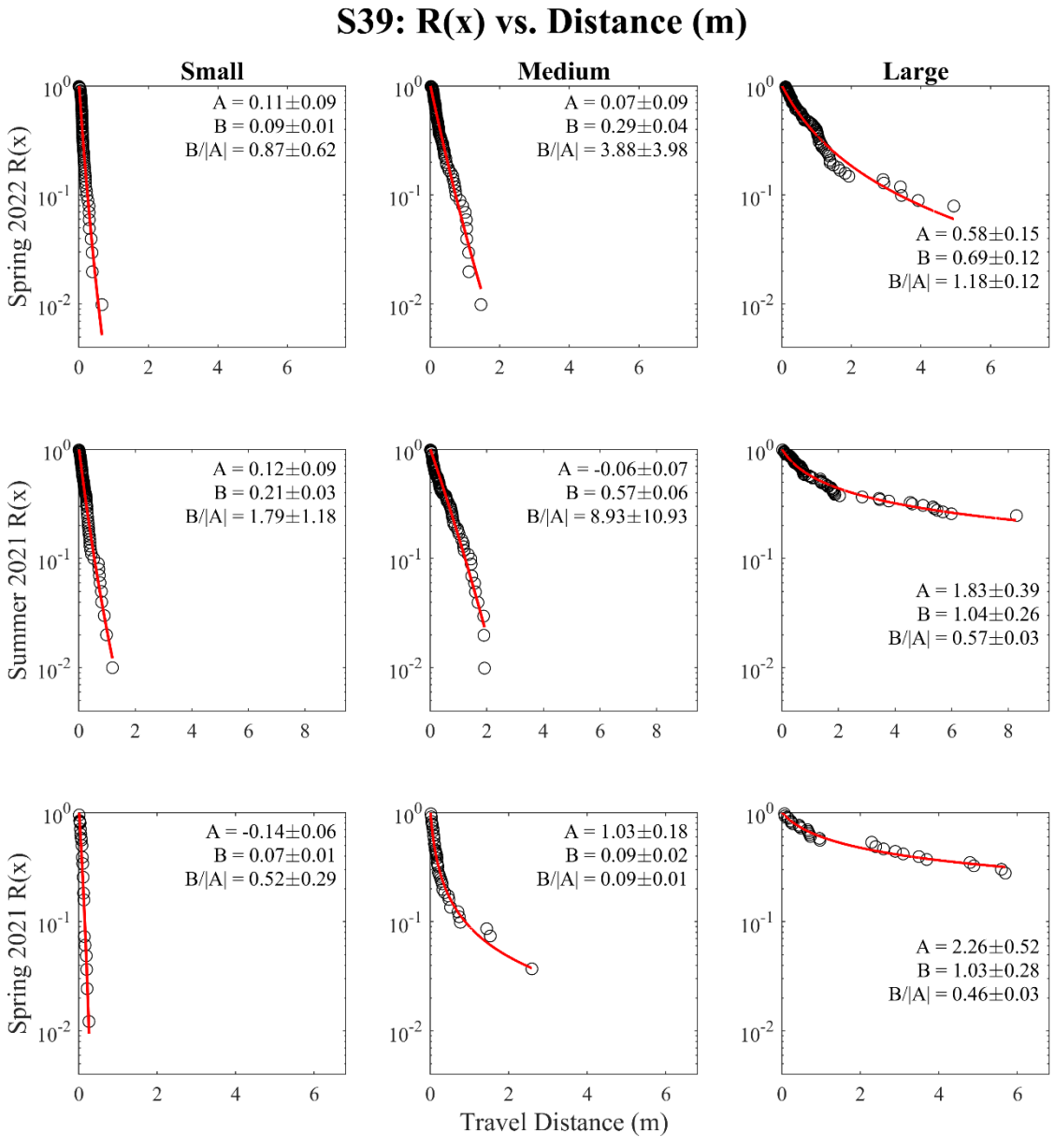

Figure B4: Empirical R(x) and modeled R(xi) for site S39 annotated with Lomax parameters A and B and characteristic distance B/|A|. Error estimations are denoted with parameter values. Black circles are empirical data.

https://doi.org/10.5194/egusphere-2023-2694
Preprint. Discussion started: 10 April 2024

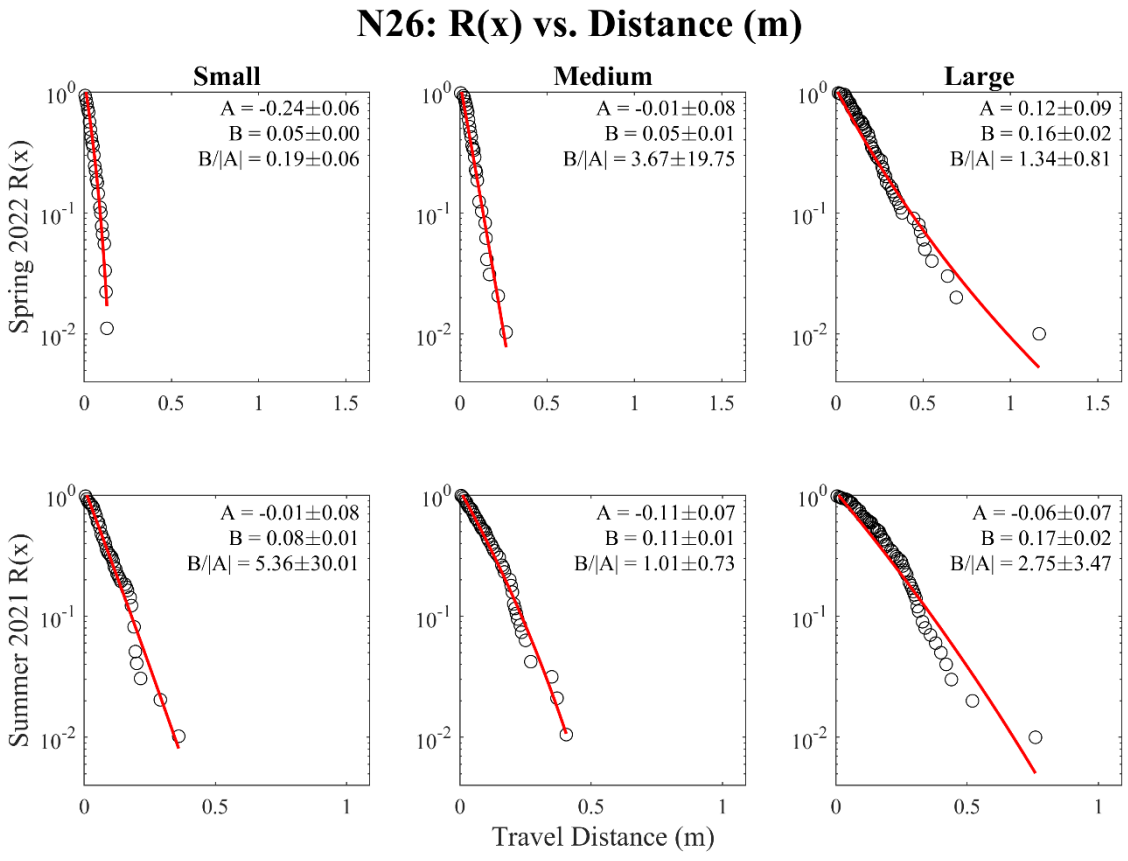

Figure B5: Empirical R(x) and modeled R(xi) for site N26 annotated with Lomax parameters A and B and characteristic distance B/|A|. Error estimations are denoted with parameter values. Black circles are empirical data.

https://doi.org/10.5194/egusphere-2023-2694
Preprint. Discussion started: 10 April 2024

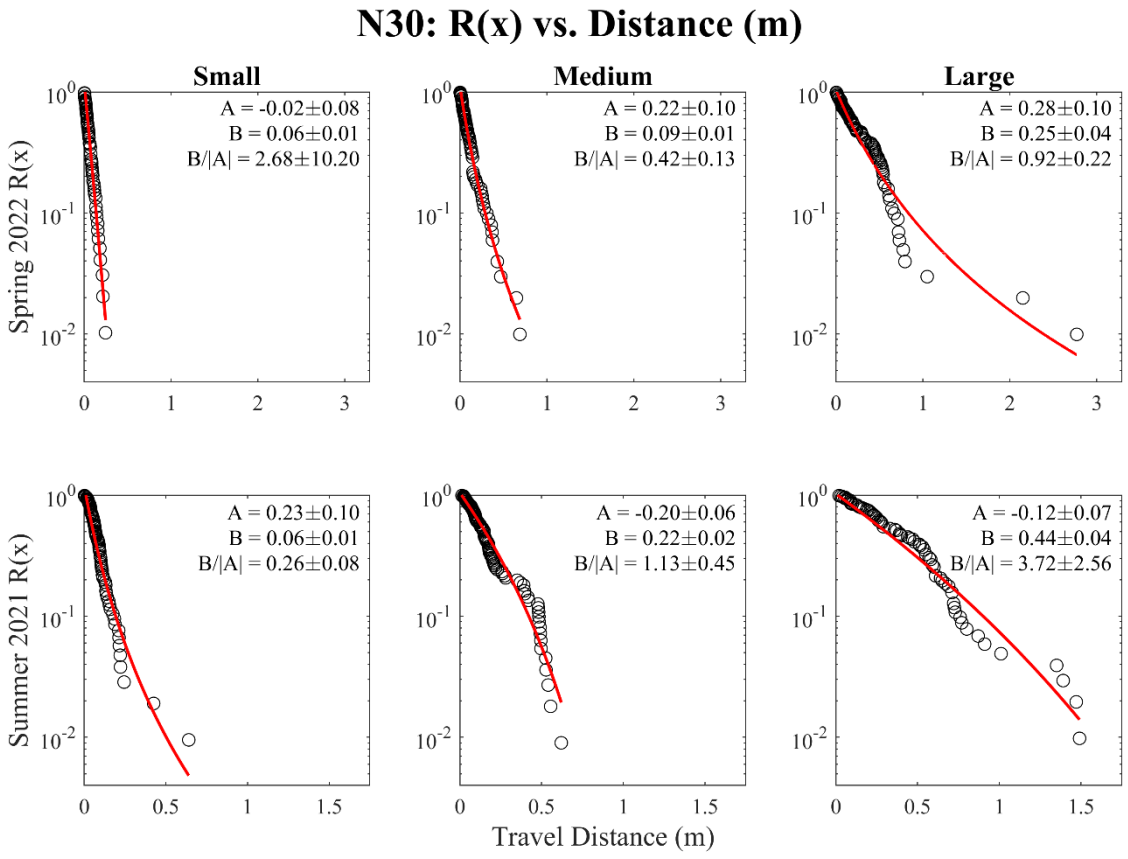

Figure B6: Empirical R(x) and modeled R(xi) for site N30 annotated with Lomax parameters A and B and characteristic distance B/|A|. Error estimations are denoted with parameter values. Black circles are empirical data.

https://doi.org/10.5194/egusphere-2023-2694
Preprint. Discussion started: 10 April 2024

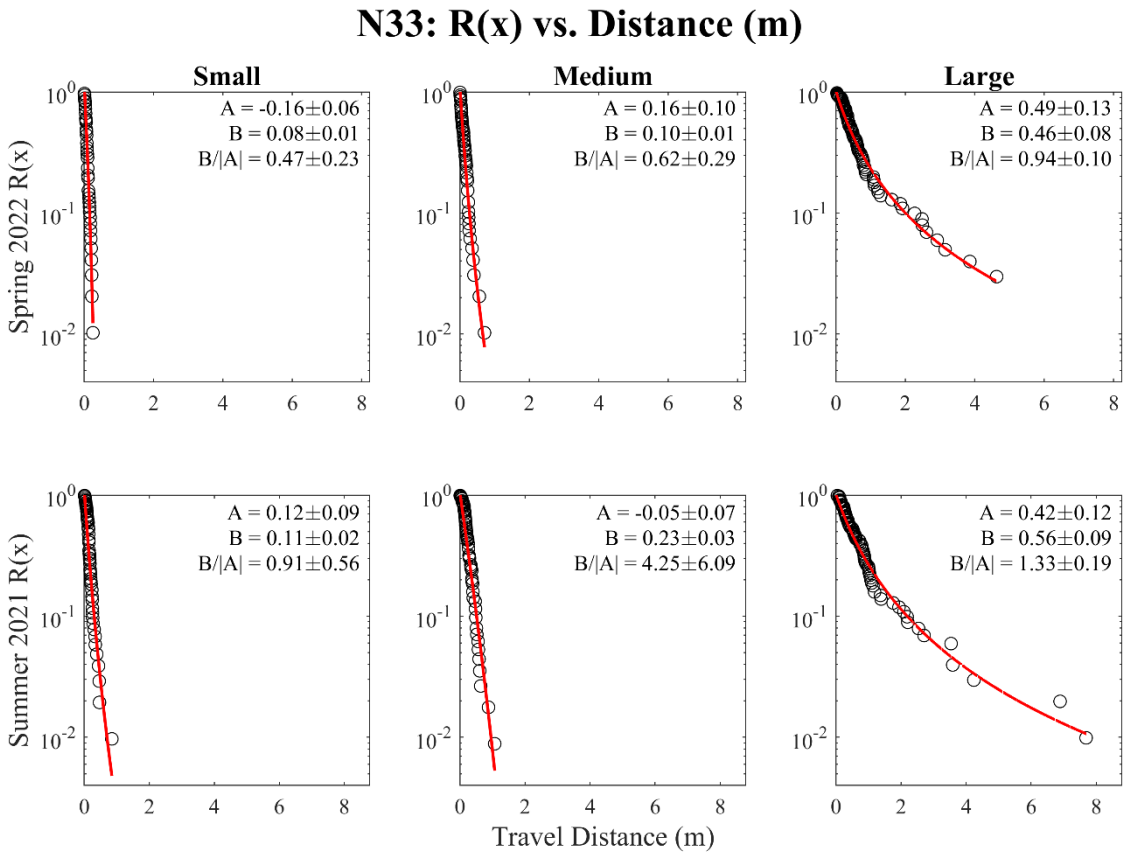

Figure B7: Empirical R(x) and modeled R(xi) for site N33 annotated with Lomax parameters A and B and characteristic distance B/|A|. Error estimations are denoted with parameter values. Black circles are empirical data.

Code and Data Availability

The V1.0.0 version of the code (Lomax2) and data (particle travel distances, Wolman counts) required to recreate the analyses presented in this manuscript can be found on Github and are archived with Zenodo (Jacobson, 2023). Topographic data are available in the UNAVCO online data archive at https://doi.org/10.7283/cp79-v370

Author Contributions

Conceptualization, D.L.R., M.Z., K.J.; Methodology, H.L.J., D.L.R., G.W.; Software, H.L.J., D.L.R.; Formal analysis, H.L.J., D.L.R., G.W.; Investigation, H.L.J., D.L.R., M.Z.; Data curation, H.L.J.; Writing – Original Draft, H.L.J.; Writing –

https://doi.org/10.5194/egusphere-2023-2694
Preprint. Discussion started: 10 April 2024

Review & Editing, H.L.J., D.L.R., G.W., M.Z., K.J.; Visualization, H.L.J.; Supervision, D.L.R., G.W.; Funding Acquisition, D.L.R., M.Z., K.J.

Competing interests

The authors declare that they have no conflict of interest.

Acknowledgements

This work was supported with National Science Foundation (NSF) Division of Earth Sciences award no. 2123220. The authors thank Zac Harlow and Zac Tuthill for assisting with site access and providing equipment at Blue Oak Ranch Reserve, part of the University of California Natural Reserve System. We greatly appreciate Amanda Donaldson, Lauren Giggy, Michael Wilshire, Nerissa Barling, and Dylan Elliott, members of the UC Santa Cruz Watershed Hydrology Laboratory, and Mel Zhang, Natalie Lasater, Stephen Gialamas, and Samantha Burton, members of the Surface Processes and Geomorphology Group at CSM, for assisting with field work and data management. Lidar acquisition services were provided by the GAGE Facility, operated by UNAVCO, Inc., with support from the National Science Foundation, the National Aeronautics and Space Administration, and the U.S. Geological Survey under NSF Cooperative Agreement EAR-1724794.

References

Bennett, K. A.: Effects of slash burning on surface soil erosion rates in the Oregon Coast Range, M.S. Thesis, Oregon State University, 1982.

Black, T. A. and Montgomery, D. R.: Sediment transport by burrowing mammals, Marin County, California, Earth Surf. Proc. Land. 16, 163–172, https://doi.org/10.1002/esp.3290160207, 1991.

Cannon, S. H., Gartner, J. E., Rupert, M. G., Michael, J. A., Rea, A. H., and Parrett, C.: Predicting the probability and volume of postwildfire debris flows in the intermountain western United States, GSA Bulletin, 122, 127–144, https://doi.org/10.1130/B26459.1, 2010.

Collins, L. and Ketcham, B.: Fluvial Geomorphic Response Of a Northern California Coastal Stream To Wildfire, 2001.

DiBiase, R. A. and Lamb, M. P.: Vegetation and wildfire controls on sediment yield in bedrock landscapes, Geophys. Res. Lett., 40, 1093–1097, https://doi.org/10.1002/grl.50277, 2013.

DiBiase, R. A. and Lamb, M. P.: Dry sediment loading of headwater channels fuels post-wildfire debris flows in bedrock landscapes, Geology, 48, 189–193, https://doi.org/10.1130/G46847.1, 2019.

https://doi.org/10.5194/egusphere-2023-2694
Preprint. Discussion started: 10 April 2024

Dibblee, T. W., and Minch, J. A. Geologic map of the Mount Day quadrangle, Santa Clara & Alameda Counties, California. Dibblee Geological Foundation, Dibblee Foundation Map DF-236, 2006.

DiBiase, R. A., Lamb, M. P., Ganti, V., and Booth, A. M.: Slope, grain size, and roughness controls on dry sediment transport and storage on steep hillslopes, J. Geophys. Res.-Earth, 122, 941–960, https://doi.org/10.1002/2016JF003970, 2017.

Donaldson, A. M., Zimmer, M., Huang, M.-H., Johnson, K. N., Hudson-Rasmussen, B., Finnegan, N., Barling, N., and Callahan, R. P.: Symmetry in Hillslope Steepness and Saprolite Thickness Between Hillslopes With Opposing Aspects, J. Geophys. Res.-Earth, 128, e2023JF007076, https://doi.org/10.1029/2023JF007076, 2023.

East, A. E., Logan, J. B., Dartnell, P., Lieber-Kotz, O., Cavagnaro, D. B., McCoy, S. W., and Lindsay, D. N.: Watershed Sediment Yield Following the 2018 Carr Fire, Whiskeytown National Recreation Area, Northern California, Earth and Space Science, 8, e2021EA001828, https://doi.org/10.1029/2021EA001828, 2021.

Florsheim, J. L., Keller, E. A., and Best, D. W.: Fluvial sediment transport in response to moderate storm flows following chaparral wildfire, Ventura County, southern California, GSA Bulletin, 103, 504–511, https://doi.org/10.1130/0016-7606(1991)103<0504:FSTIRT>2.3.CO;2, 1991.

Foufoula-Georgiou, E., Ganti, V., and Dietrich, W. E.: A nonlocal theory of sediment transport on hillslopes, J. Geophys. Res.-Earth, 115, https://doi.org/10.1029/2009JF001280, 2010.

Furbish, D. J. and Haff, P. K.: From divots to swales: Hillslope sediment transport across divers length scales, J. Geophys. Res.-Earth, 115, https://doi.org/10.1029/2009JF001576, 2010.

Furbish, D. J. and Roering, J. J.: Sediment disentrainment and the concept of local versus nonlocal transport on hillslopes, J. Geophys. Res.-Earth, 118, 937–952, https://doi.org/10.1002/jgrf.20071, 2013.

Furbish, D. J., Roering, J. J., Doane, T. H., Roth, D. L., Williams, S. G. W., and Abbott, A. M.: Rarefied particle motions on hillslopes: 1. Theory, Physical: Earth Surf. Dynam., 9, 539-576 https://doi.org/10.5194/esurf-9-539-2021, 2021a.

Furbish, D. J., Williams, S. G. W., Roth, D. L., Doane, T. H., and Roering, J. J.: Rarefied particle motions on hillslopes – Part 2: Analysis, Earth Surf. Dynam., 9, 577–613, https://doi.org/10.5194/esurf-9-577-2021, 2021b.

Gabet, E. J.: Sediment transport by dry ravel, J. Geophys. Res.-Sol. Ea., 108, https://doi.org/10.1029/2001JB001686, 2003.

Gabet, E. J. and Mendoza, M. K.: Particle transport over rough hillslope surfaces by dry ravel: Experiments and simulations with implications for nonlocal sediment flux, J. Geophys. Res.-Earth, 117, https://doi.org/10.1029/2011JF002229, 2012.

Guilinger, J. J., Gray, A. B., Barth, N. C., and Fong, B. T.: The Evolution of Sediment Sources Over a Sequence of Postfire Sediment-Laden Flows Revealed Through Repeat High-Resolution Change Detection, J. Geophys. Res.-Earth, 125, e2020JF005527, https://doi.org/10.1029/2020JF005527, 2020.

Jackson, M. and Roering, J. J.: Post-fire geomorphic response in steep, forested landscapes: Oregon Coast Range, USA, Quaternary Sci. Rev., 28, 1131–1146, https://doi.org/10.1016/j.quascirev.2008.05.003, 2009.

Jacobson, H.: Lomax2, Zenodo [code]. https://zenodo.org/doi/10.5281/zenodo.10048973, 2023.

https://doi.org/10.5194/egusphere-2023-2694
Preprint. Discussion started: 10 April 2024

Kean, J. W., Staley, D. M., and Cannon, S. H.: In situ measurements of post-fire debris flows in southern California: Comparisons of the timing and magnitude of 24 debris-flow events with rainfall and soil moisture conditions, J. Geophys. Res.-Earth, 116, https://doi.org/10.1029/2011JF002005, 2011.

Lagarias, J. C., Reeds, J. A., Wright, M. H., Wright, P. E.: Convergence Properties of the Nelder-Mead Simplex Method in Low Dimensions. SIAM J. Optimiz., 9, 112-147, https://doi.org/10.1137/S1052623496303470, 1998.

Lamb, M. P., Scheingross, J. S., Amidon, W. H., Swanson, E., and Limaye, A.: A model for fire-induced sediment yield by dry ravel in steep landscapes, J. Geophys. Res.-Earth, 116, https://doi.org/10.1029/2010JF001878, 2011.

Lamb, M. P., Levina, M., DiBiase, R. A., and Fuller, B. M.: Sediment storage by vegetation in steep bedrock landscapes: Theory, experiments, and implications for postfire sediment yield, J. Geophys. Res.-Earth, 118, 1147–1160, https://doi.org/10.1002/jgrf.20058, 2013.

Lavé, J. and Burbank, D.: Denudation processes and rates in the Transverse Ranges, southern California: Erosional response of a transitional landscape to external and anthropogenic forcing, J. Geophys. Res.-Earth, 109, https://doi.org/10.1029/2003JF000023, 2004.

Milojević, S.: Power law distributions in information science: Making the case for logarithmic binning, J. Am. Soc. Inf. Sci. Tec., 61, 2417–2425, https://doi.org/10.1002/asi.21426, 2010.

Parks, S. A. and Abatzoglou, J. T.: Warmer and Drier Fire Seasons Contribute to Increases in Area Burned at High Severity in Western US Forests From 1985 to 2017, Geophysical Res. Lett., 47, https://doi.org/10.1029/2020GL089858, 2020.

Perkins, J. P., Diaz, C., Corbett, S. C., Cerovski-Darriau, C., Stock, J. D., Prancevic, J. P., Micheli, E., and Jasperse, J.: Multi-Stage Soil-Hydraulic Recovery and Limited Ravel Accumulations Following the 2017 Nuns and Tubbs Wildfires in Northern California, J. Geophys. Res.-Earth, 127, https://doi.org/10.1029/2022JF006591, 2022.

Reed, S., and Amundson, R.: Sediment, gophers, and time: a model for the origin and persistence of Mima mound—vernal pool topography in the Great Central Valley. Vernal Pool Landscapes, 14, 15-27, S2CID 28512602, 2007.

Roering, J. J. and Gerber, M.: Fire and the evolution of steep, soil-mantled landscapes, Geology, 33, 349–352, https://doi.org/10.1130/G21260.1, 2005.

Roth, D. L., Doane, T. H., Roering, J. J., Furbish, D. J., and Zettler-Mann, A.: Particle motion on burned and vegetated hillslopes, Proc. Natl. Acad. Sci. U.S.A., 117, 25335–25343, https://doi.org/10.1073/pnas.1922495117, 2020.

Shakesby, R. A. and Doerr, S. H.: Wildfire as a hydrological and geomorphological agent, Earth-Sci. Rev., 74, 269–307, https://doi.org/10.1016/j.earscirev.2005.10.006, 2006.

Sorensen, D. C., and Moré, J. C.: Computing a Trust Region Step. SIAM J. Sci. Stat. Comp., 4, 553–572, https://doi.org/10.1137/0904038, 1983.

Swanson, F. J.: Fire and geomorphic process, Fire Regime and Ecosystem Properties, 26, 401–421, 1981.

Tucker, G. E. and Bradley, D. N.: Trouble with diffusion: Reassessing hillslope erosion laws with a particle-based model, J. Geophys. Res.-Earth, 115, https://doi.org/10.1029/2009JF001264, 2010.

https://doi.org/10.5194/egusphere-2023-2694
Preprint. Discussion started: 10 April 2024

Wentworth, C. K.: A Scale of Grade and Class Terms for Clastic Sediments, The Journal of Geology, 30, 377–392, https://doi.org/10.1086/622910, 1922.

Wolman, M. G.: A method of sampling coarse river-bed material, EOS, Transactions, American Geophysical Union, 35, 951, https://doi.org/10.1029/TR035i006p00951, 1954.

Wondzell, S. M. and King, J. G.: Postfire erosional processes in the Pacific Northwest and Rocky Mountain regions, Forest Ecol. and Manag., 178, 75–87, https://doi.org/10.1016/S0378-1127(03)00054-9, 2003.